ACS APPLIED MATERIALS & INTERFACES

Research Article

www.acsami.org

High Cycling Stability and Extreme Rate Performance in Nanoscaled $LiMn_2O_4$ Thin Films

Brecht Put,*[§,†] Philippe M. Vereecken,[§,‡] Nouha Labyedh,[§] Alfonso Sepulveda,[§] Cedric Huyghebaert,[§] Iuliana P. Radu,[§] and Andre Stesmans[†]

[†]KU Leuven, Department of Physics, Celestijnenlaan 200D and [‡]KU Leuven Centre for Surface Chemistry and Catalysis, 3001 Leuven, Belgium

[§]Imec, Kapeldreef 75, 3001 Leuven, Belgium

S *Supporting Information*

ABSTRACT: Ultrathin $LiMn_2O_4$ electrode layers with average crystal size of ∼15 nm were fabricated by means of radio frequency sputtering. Cycling behavior and rate performance was evaluated by galvanostatic charge and discharge measurements. The thinnest films show the highest volumetric capacity and best cycling stability, retaining the initial capacity over 70 (dis)charging cycles when manganese dissolution is prevented. The increased stability for film thicknesses below 50 nm allows cycling in both the 4 and 3 V potential regions, resulting in a high volumetric capacity of 1.2 Ah/cm^3. It is shown that the thinnest films can be charged to 75% of their full capacity within 18 s (200 C), the best rate performance reported for $LiMn_2O_4$. This is explained by the short diffusion lengths inherent to thin films and the absence of phase transformation.

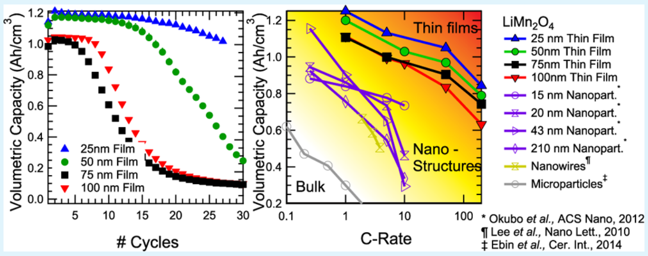

KEYWORDS: *Li-ion recharegeable battery, $LiMn_2O_4$, thin film, nanostructured, rate performance, cathode*

1. INTRODUCTION

Solid-state thin-film batteries are known to have excellent power density and are considered safer than typical liquid cells.[1−3] However, the solid-state variants currently find only limited use because of their low capacity, inherent to the use of planar thin films. The use of thicker films in solid-state devices leads to charging times beyond practical feasibility. Indeed, the large diffusion distances drastically increase the charging time. Furthermore, the intimate contact between the electrolyte and electrodes, which is easy to achieve with a liquid electrolyte, has not been demonstrated for solid-state devices. This results in only a limited active surface area in thin film devices which further increases the charging time.[4−7]

The use of three-dimensional (3D) nanostructured surfaces has been suggested to solve current thin-film battery energy deficiency.[3,4,8−10] Different structures have been investigated for this purpose, for example, silicon pillars,[1] a metal mesh,[7] silicon trenches,[10] etc.[9] By using these as a scaffold for battery fabrication, the capacity is raised without increasing film thickness. This way, a small aerial footprint and a high power output can be retained. Thin-film all-solid-state batteries provide a solution when ultrafast charging rates are required (i.e., sensors).

$LiMn_2O_4$ is among the most interesting electrode candidates because of its low cost and low toxicity, its high voltage, omnipresent lithium diffusion pathways, and finally a high gravimetric and volumetric energy density.[10−12] $LiMn_2O_4$ can intercalate two Li^+ ions into the spinel host structure. One Li^+ is incorporated at the 4 V (vs Li^+/Li) plateau, corresponding to a capacity of 633 mAh/cm^3 (148 mAh/g). Another Li^+ can be intercalated at 3 V leading to a total capacity of 1.2 Ah/cm^3 (296 mAh/g). However, intercalating two Li^+ ions leads to a volume expansion of more than 5% (and a 16% change in the crystal axis (c/a) ratio).[13,14]

At present, only the 4 V region is used in practical applications limiting the capacity to 0.6 Ah/cm^3. The reason is the intolerable volume expansion associated with the 3 V region, which results in the formation of cracks and pulverization of the material. Eventually, contact with the current collector is lost ending battery functionality.[15−17] For this reason the application of $LiMn_2O_4$ is limited to the 4 V region, but even here the cyclability is limited. Typical causes are dissolution of manganese in the electrolyte, Jahn−Teller distortion, and instability of the liquid electrolyte.[12,17,18]

Different methods have been applied to stabilize the $LiMn_2O_4$, both the 3 and 4 V plateaus. These can be divided into three large groups, namely, stabilizing by nanostructuring, coating, and doping of the material. Typical examples of the latter method are introducing, for example, Al, Ni, Co, and Li in the $LiMn_2O_4$.[18−21] This has proven successful in stabilizing the

Received: July 16, 2015
Accepted: September 11, 2015
Published: October 5, 2015

DOI: 10.1021/acsami.5b06386
ACS Appl. Mater. Interfaces 2015, 7, 22413−22420

material by changing the oxidation state of the manganese. However, typically a price is paid by a reduction in capacity. A different approach is the coating of the $LiMn_2O_4$ with, for example, Au and $Li_4Ti_5O_{12}$.[22,23] These typically improve cyclability of the material and in some cases increase the rate performance.

Recently, it has also been shown that sizing the $LiMn_2O_4$ to the nanoscale regime increases the stability and rate performance.[24] Typical nanostructures that are reported include nanoparticles,[25,26] nanorods,[27] and nanowires.[28,29] Generally, nanoscaling leads to increased stability in the 4 V region. However, a reduction in capacity is found due to the high surface-to-volume ratio of these structures.[25] Moreover, cycling stability in the 3 V region is not sufficiently improved to sustain long-term usage. Also nanoporous $LiMn_2O_4$ has been fabricated, stabilizing the 3 V region. However, it leads to a significant reduction in volumetric capacity.[30,31]

Thin films have a characteristic length scale at which nanoscale effects show up.[32−34] These have been frequently investigated in nanoparticle systems.[25,35,36] However, little is known on the onset of these phenomena in nanocrystalline thin films. Typical effects to be expected are increased lithium loading and a shift in the energy distribution of lithium intercalation sites. These phenomena can play a key role in 3D structured thin-film batteries.[37,38]

In this work, we report radio frequency (RF) sputtered thin films of $LiMn_2O_4$ achieving high cycling stability and extreme rate performance. Films with a nominal thickness ranging from 25 to 100 nm are investigated. To our knowledge these are the thinnest $LiMn_2O_4$ films evaluated, exhibiting the best rate performance reported. The films are of typical thickness expected to be used in 3D batteries.[38] Therefore, this work can serve as a model system to study these kinds of layers and the expected nanoscale effects. It can also function as a model system for a nanoparticle-based battery.

2. RESULTS AND DISCUSSION

Figure 1 shows the X-ray diffraction (XRD) results of RF-sputtered $LiMn_2O_4$ films after annealing at 800 °C. All films crystallize into the $LiMn_2O_4$ spinel structure (*Fd3m* space group). The $LiMn_2O_4$ diffraction peaks are identified in accordance with JCPDS entry No. 35−0782. Substrate materials (Pt and TiO_2) are also indicated on the XRD pattern, with the TiO_2 originating from the oxidation of the TiN adhesion layer. No impurity phases are detected.

With decreasing film thickness an increase in the $LiMn_2O_4$ peak width can be seen, indicating a decrease of the crystallite size. The Scherrer formula was used to obtain an estimation of the crystallite size for the different films (using the (111) peak).[39,40] The results are summarized in Table 1. The crystallite size ranges from 20 to 14 nm, with the thinnest film possessing the smallest crystallites. From the XRD data also the lattice parameter was calculated. This is directly correlated with the stoichiometry of the deposited film.[18] Values close to 8.24 Å are found here, agreeing well with values reported elsewhere.[41,42] This shows that the stoichiometry of the deposited films is close to the ideal value of $LiMn_2O_4$.

To further elucidate the film characteristics, Rutherford backscattering (RBS) was used to determine the absolute amount of manganese in the films. Table 1 shows the RBS thickness of the layers, calculated based on the atomic aerial density (atoms per square centimeter) and the $LiMn_2O_4$ mass density (4.28 g/cm^3).[43] The calculated thicknesses correspond well to the values obtained from scanning electron microscopy (SEM) and profilometry, indicating the films are dense. The RBS thickness was used for all normalization purposes and calculations of theoretical capacity and C-rates in this work.

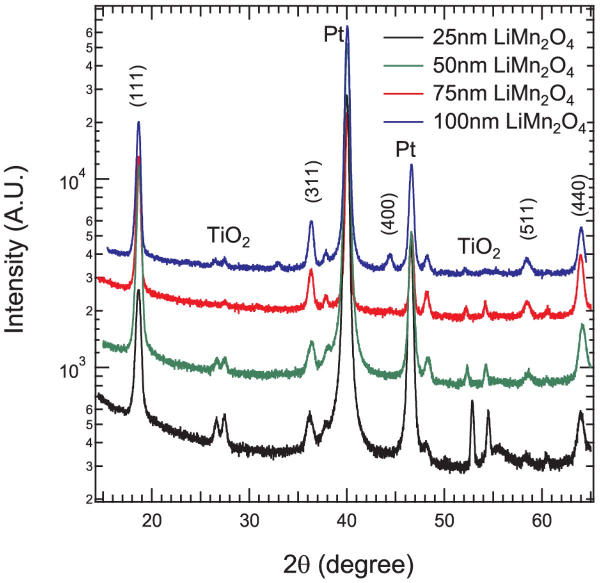

Figure 1. XRD patterns of $LiMn_2O_4$ films with varying thickness after annealing at 800 °C. The spectra correspond to the 25, 50, 75, and 100 nm layers from bottom to top respectively. All films have the spinel structure after annealing. Different crystal planes are indicated in the figure. An increase in peak width can be seen upon downscaling the film thickness. Peaks due to different substrate materials are labeled accordingly.

Table 1. Characteristics of $LiMn_2O_4$ Films with Varying Thickness after Annealing at 800° C

$LiMn_2O_4$ thickness	crystal size (nm)	lattice parameter (XRD, Å)	RBS thickness (nm)	Li/Mn ratio (ERD)
25 nm	14	8.24	30	0.6
50 nm	20	8.26	54	
75 nm	20	8.23	97	
100 nm	18	8.23	117	0.62
ideal		8.24		0.5

Finally, the stoichiometry of the films was determined by elastic recoil detection (ERD). This technique is similar to RBS. However, while RBS's sensitivity is highest for heavy atoms, ERD is most sensitive for light elements. This makes it ideally suited to measure the Li content in the films. The Li/Mn ratio obtained from ERD is also shown in Table 1. The value of ∼0.6 indicates that the films have an excess of lithium (or are Mn deficient). This discrepancy has been observed before for sputtered $LiMn_2O_4$ thin films.[44] Hence, our films have a stoichiometry of the form $Li_{1+x}Mn_{2-y}O_4$, with x, $y \approx 0.1$, attributed to preferential sputtering.

Figure 2 shows the morphology of the layers as determined by SEM. In image (a), a cross section of a 100 nm $LiMn_2O_4$ layer before anneal can be seen. A dense, uniform layer is present on top of the platinum current collector. Figure 2b shows a top view picture of the surface of a 75 nm layer after annealing. Again a uniform, closed film of $LiMn_2O_4$ can be seen. A clear distribution in the grain size is visible, with grains ranging from 10 to 200 nm. When going to thinner films the

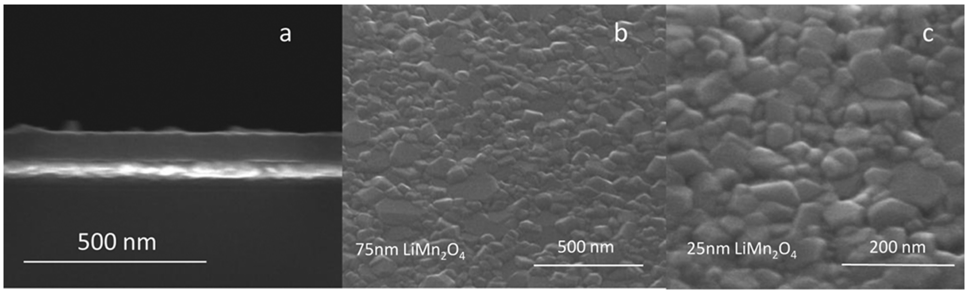

Figure 2. (a) Cross-section SEM showing the typical stack used in this work. A 100 nm uniform and dense $LiMn_2O_4$ film in good contact with the Pt current collector can be seen. (b) Top view SEM of a 75 nm $LiMn_2O_4$ layer after annealing. A uniformly closed film can be seen, composed of crystallites with a broad size distribution. (c) Top view SEM of a 25 nm $LiMn_2O_4$ layer after annealing. The film is composed of closely interconnected small crystallites. The platinum current collector, which has brighter contrast, cannot be seen.

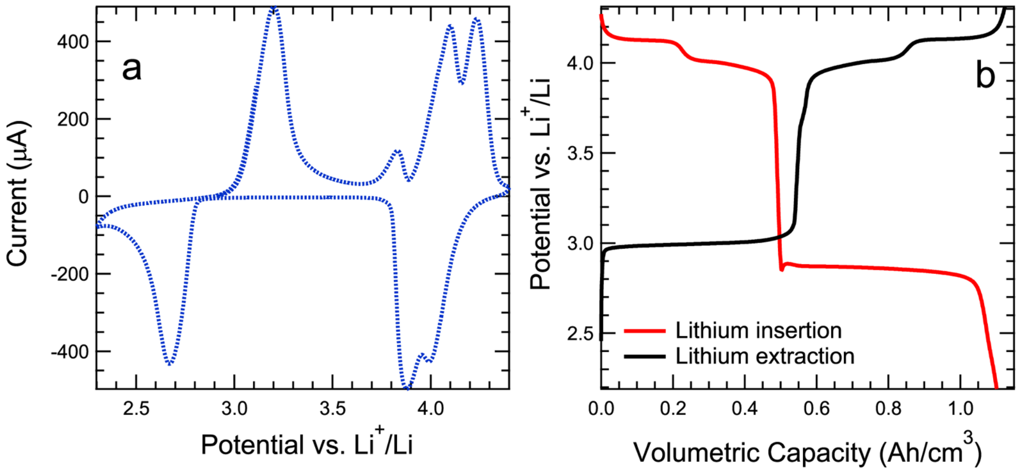

Figure 3. (a) Cyclic voltammogram of a 100 nm $LiMn_2O_4$ film showing the distinct lithium intercalation peaks around 3 V and the double peaks at 4 V (scan rate 10 mV/s). (b) Charge−discharge curves taken at 1 C (1.2 A/cm^3) in the range of 2−4.3 V vs Li^+/Li for a nominal 100 nm $LiMn_2O_4$ layer. The volumetric capacity was calculated from the RBS thickness, which is 117 nm.

crystallite distribution becomes smaller, with grains in the range of 10−50 nm forming the majority (as shown in Figure 2c).

Additional SEM images of the 50 and 100 nm $LiMn_2O_4$ layers are available in the Supporting Information Figure S1a,b. Again a distribution in the crystallite sizes is visible with grain diameters ranging between 10 and 200 nm for both films. However, the size distribution again narrows for the thinner film where a larger fraction of small particles becomes apparent.

The crystallite sizes seen here seem to contradict with the values determined from XRD. It is known that the XRD peak width will be dominated by the signal from the smaller crystallites. The increasing number of small crystallites for thinner films will therefore result in an increasing peak width. As is seen from SEM larger crystallites can still be present. Furthermore, it has been reported before that $LiMn_2O_4$ grains can be composed of multiple crystallites. In that case, domain boundaries are present in these grains.[14,34]

$LiMn_2O_4$ can intercalate two Li ions into its crystal structure. One Li ion is inserted in the 3 V region (and typically measured between 2 and 3.5 V vs Li^+/Li) and one at 4 V (accessed between 3.5 and 4.3 V vs Li^+/Li). In a cyclic voltammogram (cf. Figure 3a) this translates into characteristics peaks around 3 V and a double peak around 4 V versus Li^+/Li. Indeed, typically $LiMn_2O_4$ electrodes are evaluated only in the 4 V range to avoid degradation of the material. The rapid deterioration of the $LiMn_2O_4$ electrode system in the range of 2.0−3.0 V is caused by different reasons, the main one being the Jahn−Teller distortion.

In the present work, the Li ion storage capacity of the films was evaluated by galvanostatic charge−discharge measurements, plotted as the potential during Li ion insertion/extraction versus the lithium ion capacity (see Figure 3b). During these experiments the potential is allowed to change between 4.3 and 2 V versus Li^+/Li. Upon insertion of Li ions, the potential evolves from 4.3 to 2 V. During this variation distinct plateau regions are seen at 4.1, 4.0, and 3.0 V. Upon extracting lithium the inverse is seen.

$LiMn_2O_4$ allows the insertion of two Li ions into its structure. The double plateau at 4.1−4.0 V corresponds to Li^+ insertion into the Mn_2O_4 lattice up to $LiMn_2O_4$ (filling of the tetrahedral spinel crystal sites). This results in the maximum possible Li ion capacity of 0.6 Ah/cm^3. The plateau splitting in two smaller subplateaus can be attributed to a rearrangement of the lithium once a stoichiometry around $Li_{0.5}Mn_2O_4$ is reached. The plateau at 3 V is attributed to Li^+ loading up to $Li_2Mn_2O_4$ (filling of the octahedral crystal sites), corresponding to another 0.6 Ah/cm^3. This leads to a combined theoretical capacity of 1.2 Ah/cm^3. Attaining this full capacity has proven impossible in bulk material due to the instability of the electrode material at 3 V.[12] As such bulk $LiMn_2O_4$ is only used in the 4.0 V region.

Figure 4 shows the results of constant current charge−discharge experiments on $LiMn_2O_4$ with varying thickness (only showing the discharge curves). The evolution of the

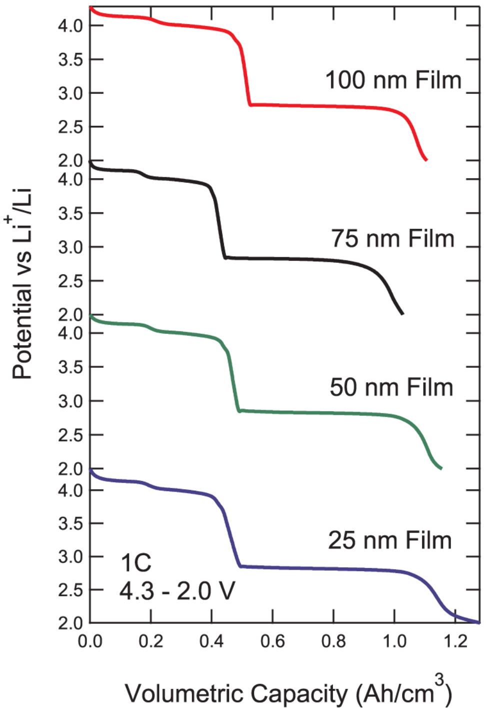

Figure 4. Discharge curves taken at 1 C (1.2 A/cm^3) in the range of 2−4.3 V vs Li^+/Li for $LiMn_2O_4$ layers with different thickness. The volumetric capacity is highest for the thinnest film. The latter film allows Li ion loading up to $Li_2Mn_2O_4$, corresponding to a capacity of 1.2 Ah/cm^3. The volumetric capacity was calculated from the RBS thickness: 30, 54, 97, and 117 for the 25, 50, 75, and 100 nm nominal films.

potential during the third discharge cycle is shown here. The volumetric capacity was calculated using the RBS thickness of the film. The charging rate during these measurements was 1 C, which is equal to charging the film to its full maximum theoretical charge in 1h, or a current of 1.2 A/cm^3.

Interestingly, the total volumetric capacity of all the layers approaches the full theoretical value of 1.24 Ah/cm^3. For the thinnest film even 100% of the theoretical capacity was measured in several cases. To our knowledge, this is the first observation of 100% capacity in thin films (see Supporting Information Figure S2 for more details on capacity of the 3 V and the 4 V regions.). The results are in good accordance with the phase diagram published by Okubo et al.,[25] which predicted stoichiometries as high as $Li_{2.5}Mn_2O_4$ can be obtained in nanoscaled $LiMn_2O_4$. Similar effects have been reported in TiO_2.[35]

Upon closer investigation of Figure 4 both the capacity in the 4 and 3 V region is seen to vary with film thickness. The 100 nm layer shows the largest Li ion insertion capacity in the 4 V region of the investigated films. While in the 3 V region the largest insertion capacity is found for the thinnest film. The effect of the varying IR drop on the films was examined but failed to account for the variations in capacity.

The variation of the Li ion capacity with grain size in the 4 V region is a known effect in nanoparticle systems. This capacity typically decreases with decreasing particle size, which is attributed to an increased surface to volume ratio for smaller particles. This causes a shift in the distribution of the energy states of Li^+ intercalation sites resulting in a decreased capacity. The effect can be explained and modeled by the lattice gas model.[45]

The capacity of the 3 V region is found to be largest for the 25 nm film. However, no linear dependency on film thickness is observed. Different factors like grain size and distribution and film thickness influence the variation of the capacity. Furthermore, it is known that smaller crystallites allow higher lithium stoichiometry (up to $Li_{2.5}Mn_2O_4$) and do not show typical Li ion intercalation behavior. Instead, they store lithium through the formation of a solid solution. This typically is a faster process, because of the absence of phase boundaries. Therefore, also reaction kinetics might play a role in these measurements. The combined effect of the above factors prevent straightforward interpretation of the dependency of the 3 V capacity on film thickness. Furthermore, the complex interplay of the increasing 3 V capacity and decreasing 4 V capacity might explain why here the lowest capacity is found for the 75 nm film.

As mentioned before, $LiMn_2O_4$ is generally only evaluated in the 4 V potential region. Because of the rapid degradation of the material in the 3 V region, the potential window is typically restricted above 3.5 V. In what follows the cyclability of the $LiMn_2O_4$ thin films is evaluated between 2 and 4.3 V versus Li^+/Li, giving rise to a theoretical capacity of 1.2 Ah/cm^3.

To test the cyclability of the material again constant current charge−discharge measurements at 1 C were conducted. Figure 5 shows the results of these experiments. The 100 and 75 nm films degrade rapidly when cycled in the full potential range; 50% of the initial capacity is lost after 10 cycles. This is in line with previous reports on submicron thick films. It is typically attributed to mechanical degradation of the material due to the Jahn−Teller distortion.

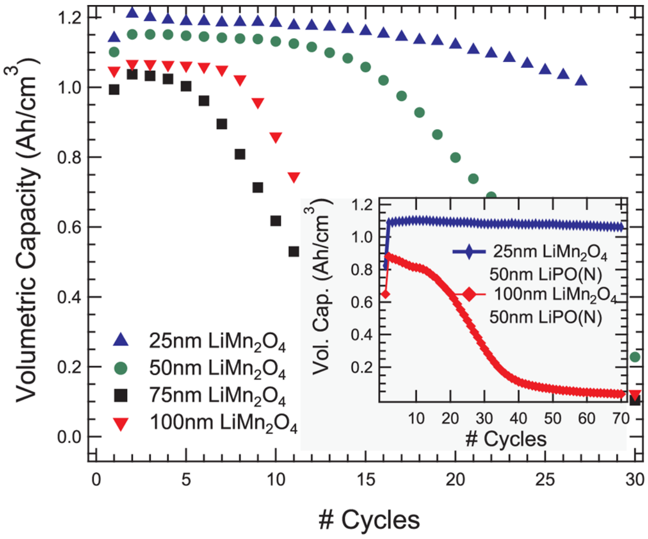

Figure 5. Volumetric capacity vs cycle number for films cycled at 1 C in the potential region from 2−4.3 V vs Li^+/Li. Thinner films are stable over prolonged cycling, while thicker films rapidly degrade. (inset) The behavior of $LiMn_2O_4$ with a 50 nm LiPON layer on top. The thinnest layer remains stable over prolonged cycling hardly losing any capacity. The thicker layer rapidly loses its capacity.

Upon downscaling the film the volumetric capacity and cyclability of the 25 and 50 nm films increases. The 25 nm film can be seen to be stable over prolonged cycling, retaining ∼85% of its capacity at the end of the cycling period. However, this degradation is not due to mechanical damage but can be attributed to the dissolution of manganese into the liquid

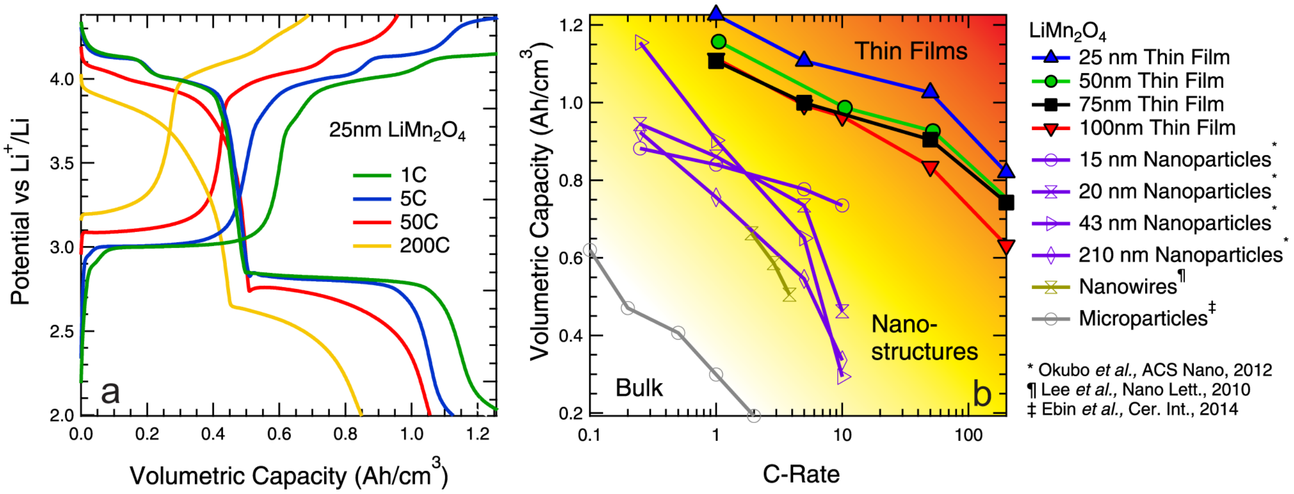

Figure 6. (a) Charge−discharge curves for 25 nm LiMn$_2$O$_4$ layer. The layer shows excellent rate performance together with a high charging and discharging capacity. (b) Volumetric (lithiation) capacity vs C-rate for films with different thickness. All films show excellent rate performance retaining over 80% of their 1 C capacity while charging in 1.2 min (50 C). Other structures from literature are shown for comparison.[25,29,52]

electrolyte, a known problem for LiMn$_2$O$_4$.[12,22] Because of the dominance of such dissolution mechanism cycling experiments were not conducted above 30 cycles. Furthermore, in present work the focus is on layers for use in an all-solid-state thin-film battery. For this reason, the influence of manganese dissolution was prevented by adding a protective LiPON layer (50 nm, N-doped Li$_3$PO$_4$ glass, see Supporting Information Figures S3 and S4) on top of the LiMn$_2$O$_4$. Only a thin LiPON layer was used here to prevent reductions in the 1 C capacity caused by kinetic limitations of the solid electrolyte.

The inset of Figure 5 shows an enhancement of cycling stability of these films. Upon covering the 25 nm LiMn$_2$O$_4$ layer, it remained extremely stable for all 70 cycles measured and retained its full capacity. For the 100 nm films coated with 50 nm LiPON the cyclability did not improve considerably, as capacity dropped steeply after 10 cycles. Degradation in these thicker films was slower than without the protective LiPON layer but still occurs rapidly. This can be explained by the volume expansion of the LiMn$_2$O$_4$, which cracks the protective LiPON layer and allows dissolution of the exposed LiMn$_2$O$_4$ in the liquid electrolyte.

The Coulombic efficiency of the cycled films was also investigated. All of the blank LiMn$_2$O$_4$ films initially showed an efficiency of ~90%, which dropped together with the capacity to ~80%. The limited efficiency of the blank films originates from the onset of solvent decomposition at the high potentials employed here. However, when the material was protected by the LiPON layer the Coulombic efficiency for the thinnest LiMn$_2$O$_4$ film remained between 98.8 and 99.1%. In the 100 nm film again the efficiency reduced together with the capacity and dropped to 93%.

To our knowledge, this is the first time that stable cycling behavior has been shown for thin LiMn$_2$O$_4$ films in the full potential range of 2−4.3 V versus Li$^+$/Li while attaining full theoretical capacity (intercalating two Li$^+$ ions).

When LiMn$_2$O$_4$ is used in the potential full range, all of the manganese reaches oxidation state +III upon full lithiation. A majority of Mn (III) over Mn (IV) results in the onset of the Jahn−Teller distortion, which is associated with a phase transformation leading to a volume change of 5% and a variation of 16% in the *c*/*a* ratio.[13] This introduces large mechanical stresses in the system. The increased stability of the investigated thin films may have different origins.

Generally the study of stress and strain formation in thin films is done by separating the surface and bulk, and picturing them as two distinct layers on top of each other.[46,47] This is due to the different response to stress of the material close to a free surface. This layered picture is remarkably accurate in case of progressive lithiation. The top part of the electrode intercalates first and undergoes the Jahn-teller distortion and the associated phase transformation. This results in two distinct regions with different lattice constants, leading to a buildup of stress in the layer. However, because of the limited thickness of the thin films, formation of two distinctly different layers in close contact is unlikely. In the case of ultrathin films, a situation similar to nanowires arise due to the close proximity of the free surface. Nanowire structures are known to efficiently relax stresses to their surface leading to defect-free epitaxial interfaces.[48−50]

When bulk material is used distinct layers will form leading to compressive stress in the surface layer and tensile stress in the bulk. This typically results in mechanical degradation of the material. Compared to bulk material (both thick films as well as large particles), thin films allow easier relaxation of stress and accommodation of volume changes by the swelling of the layer.[46] Furthermore, since thin films are used in this work, the absolute volume changes remain limited. Increases in stability upon downscaling have also been observed in thin film silicon electrodes.[51]

An additional effect of downscaling the film thickness (and the associated reduction in crystal size) is the change of Li ion storage mode. While for large crystallites lithium is stored by intercalating into the LiMn$_2$O$_4$ lattice, for grains smaller than 15 nm lithium is thought to be stored through a solid solution regime without domain boundaries.[25] This lithium storage mode will significantly improve cyclability due to the absence of a phase change. It has been reported that the detrimental *c*/*a* axis elongation of 16% is absent in case of solid solution formation.[25]

Another contribution to the cyclability of the films originates from its polycrystalline nature. From Figure 2 and the values of the grain size in Table1, it can be noticed that the films investigated here constitute a large number of grain boundaries.

The concurrent motion of these grain boundaries on experiencing volume changes is known to help to alleviate stresses. This leads to an increased cyclability of the material.[20]

A final reason for the increased stability is the film off-stoichiometry (as shown in Table 1). The investigated films have a composition of the form $Li_{1+x}Mn_{2-y}O_4$. Because of the lower manganese content, also with respect to oxygen, the average oxidation state of the manganese is increased. This results in a slightly lower capacity in the 4 V region; however, it delays the onset of the Jahn–Teller distortion.[18] The excellent cycling stability of the investigated $LiMn_2O_4$ thin films is likely a combination of the different mechanisms described here.

Thin films inherently have a short diffusion length, which makes them ideally suited for high rate/high power batteries. Typically, this is probed in function of the C-rate (1 C is charging/discharging the battery to full theoretical capacity of 1.24 Ah/cm^3 in 1 h. This corresponds to a current of 1.24 A/cm^3).

Figure 6a shows the constant current charge–discharge curves at different C-rates of the 25 nm film. Its superior rate performance is demonstrated here. The film retains over 80% of the theoretical capacity when discharging at 50C. Also its excellent volumeteric capacity is noted, reaching close to 100% of the theoretical value at 1C. Note that at low C-rates lithiation was completed before the cutoff value of 4.3 V due to low internal IR-drop.

From Figure 6a it is also seen that the 4 and 3 V plateaus have different rate performances. The capacity under the 4 V plateau remains unchanged up to 50 C and still is at 90% at 200 C. The main drop in total capacity with increasing C-rate originates from the 3 V plateaus. This has been described before and is due to the lower diffusion constant in highly lithiated $LiMn_2O_4$.[53]

Figure 6b summarizes the lithiation capacity of our films with different thickness between 25 and 100 nm and makes a comparison with literature structures tested in the full potential range (2–4.3 V).[25,29,52] It is seen that the 25 nm film retains over 70% of its full theoretical capacity at 200 C (charging in 18 s). The other films (50, 75, and 100 nm) had a lower starting capacity but still show exceptionally good rate performance. All of the films retain more than 75% of the maximum theoretical capacity at 10 C (charged in 6 min). Only the 100 nm film shows a slightly larger capacity drop at high C-rate. To exclude the effect of degradation in the films above 50 nm, the high C-rate measurements were measured in random sequence and interspersed with charge–discharge experiments at 1 C. These 1 C values were then compared with the initial characterizations. Once these 1 C values differed significantly (more than 15%) the measurement was stopped and the sample was discarded.

When comparing our rate performance with that reported for nanoparticles,[25] nanowires,[29] and microparticles.[52] It is clear that thin films outperform the other morphologies both in capacity and rate performance. At 10 C the nanoparticles lose over 50% of their maximum capacity (measured at 0.25 C). The thin films shown here still retain over 85% of their maximum capacity (measured at 1 C) and more than 75% of the full theoretical capacity. Only the 15 nm nanoparticles show rate dependency similar to the thin films. They retain 80% of their maximum capacity (measured at 0.25 C) when charging at 10 C. However, their initial capacity is only 75% of the starting capacity in our thin films. The nanowires show similar behavior to the nanoparticle structures (all but the 15 nm particles).[29] The microparticles, which act similar to bulk material, only reach approximately half the full theoretical capacity at 0.1 C (0.6 Ah/cm^3) when measuring in the full potential range. Upon increasing the scan rate to 2 C, the capacity rapidly drops to 30% of the initial value.[52]

The excellent performance of the thin films of $LiMn_2O_4$ is due to several factors, the first one being that thin films form intimate contact with the current collector, whereas powder coatings rely on contact between mixed in carbon black. In the nanoparticle systems plotted in Figure 6, already 20 wt % of carbon black is used. However, good contact cannot always be guaranteed even when 45 wt % is used in powder coatings.[36]

Second, our films have an average grain size of 14–20 nm (see Table 1). It was reported before that nanoparticles with a 15 nm diameter are thought to show a solid solution-like behavior. The potential evolution curves reported here closely resemble those for solid solution behavior shown elsewhere.[25] The absence of phase nucleation, which is typically a rate-limiting step, thus greatly affects rate performance.[25,35,36]

To conclude the rate performance of a 25 nm $LiMn_2O_4$ layer with a 50 nm protective LiPON layer was tested (Supporting Information Figure S5). A reduction of the rate performance can be seen compared to the unprotected $LiMn_2O_4$ due to the use extra resistance of the solid electrolyte. However, the thin LiPON layer still allows charging to 75% of the maximum capacity at 10 C and thereby still outperforms the nanostructures shown in Figure 6b. Furthermore, it proved stable over prolonged cycling. Clearly usage of electrolytes with higher ionic conductivity, for example, $Li_{3x}La_{2/3-x}TiO_3$,[54] will improve the stack's rate capability and facilitate the optimal $LiMn_2O_4$ rate performance shown in Figure 6.

3. CONCLUSION

We have shown the use of ultrathin $LiMn_2O_4$ films as enabler for ultrafast charging battery applications. The fabricated films have an average crystal size ranging between 14 and 20 nm. The thinnest films (25 and 50 nm) reported here reach ∼100% of the full theoretical capacity (1.2 Ah/cm^3). This high capacity originates from cyclability in both the 3 and 4 V potential region thereby enabling full usage of the $LiMn_2O_4$ (intercalating two Li^+ ions). Stable cycling has been shown for the thinnest films retaining their full capacity over 70 cycles when manganese dissolution is prevented. The reported layers enable extreme charging rates, retaining over 80% of the theoretical capacity at 50 C. These films thereby outperform other nanostructures both in capacity as in rate performance.

However, because of their limited thickness the total storage capacity of thin films remains limited. Therefore, these must be combined with large-area structures like Si pillars, anodized aluminum templates, etc. Area increases of 100–1000 can hereby be realized. This brings the performance of these thin film batteries in the range of classical liquid lithium cells. However, because of the fast charging rates, enabled by the use of thin films, charge can be resupplied much faster. This can enable numerous applications (e.g., fast-charging EVs). It can even reduce the need for high-capacity batteries since recharging proceeds much faster, making frequent charging much less disturbing for the user.

4. EXPERIMENTAL SECTION

$LiMn_2O_4$ films were deposited by RF-sputtering from a 4 in. target (Neyco, France, 99.5% purity). The deposition was done at 100 W of power and under Ar flow of 25 sccm. As substrate a silicon wafer with a stack of 10 nm TiN (ALD) on 30 nm thermally grown silicon oxide was used. This stack received a preanneal at 800 °C in ambient for 30 min. This was done to prevent outgassing during later processing. On this stack, 80 nm platinum was deposited by DC sputtering, which is later on used as current collector. Finally, the $LiMn_2O_4$ layer was deposited by RF sputtering. As deposited, the layers were amorphous and inactive; therefore, a post-deposition annealing was performed. This was done for 20 min at 800 °C in oxygen atmosphere (Annealsys).

The morphology of the deposited layers was checked with SEM (Nova). Crystallinity of the films was checked with X-ray diffraction (X'pert Panalytical) using Cu Kα radiation in grazing incidence configuration. Rutherford backscattering was used to determine an RBS thickness (together with the ideal mass density). During the RBS measurements a He^+ beam is accelerated to an energy of 1.52 MeV and scattered of the film. The backscattered ions are detected by a time-of-flight energy (TOFE) telescope. The film stoichiometry was determined by ERD. In the ERD experiments, a primary ion beam of Cl^+ is accelerated to 6 MeV by a 2 MV tandem accelerator. The forward recoiled and scattered ions are detected with a TOFE telescope.

All electrochemical experiments were done in an Ar glovebox (O_2, $H_2O < 1$ ppm). A three-electrode Teflon cell was clamped on top of the sample using a Kalrez O-ring. A Luggin capillary made connection between the cell and the reference electrode compartment. A detail of the setup is show in the Supporting Information (Figure S6). One molar $LiClO_4$ (battery grade, Sigma-Aldrich) in propylene carbonate was used as electrolyte. An autolab (Metrohm) potentiostat was used for all testing operated by Nova software (Metrohm Autolab).

■ ASSOCIATED CONTENT

Supporting Information

The Supporting Information is available free of charge on the ACS Publications website at DOI: 10.1021/acsami.5b06386.

> A plot of the variation of the 4 V, 3 V, and total capacity for the different samples measured, SEM images of 50 and 100 nm layers, data plotted for characterization of the LiPON used to protect the $LiMn_2O_4$ layers, and a figure showing the rate dependence of the LiPON/ $LiMn_2O_4$ stack. To conclude, a sketch of the electrochemical cell used in this work is present. (PDF)

■ AUTHOR INFORMATION

Corresponding Author

*E-mail: brecht.put@imec.be.

Notes

The authors declare no competing financial interest.

■ ACKNOWLEDGMENTS

The authors thank M. Lux for providing the SEM and J. Meersschaut for the ERD and RBS characterizations.

■ REFERENCES

(1) Vereecken, P. M.; Huyghebaert, C. Conformal Deposition For 3D Thin-Film Batteries. *ECS Trans.* **2013**, *58*, 111−118.

(2) Patil, A.; Patil, V.; Shin, D. W.; Choi, J.-W.; Paik, D.-S.; Yoon, S.-J. Issue and challenges facing rechargeable thin film lithium batteries. *Mater. Res. Bull.* **2008**, *43*, 1913−1942.

(3) Baggetto, L.; Niessen, R. A. H.; Roozeboom, F.; Notten, P. H. L. High Energy Density All-Solid-State Batteries: A Challenging Concept Towards 3D Integration. *Adv. Funct. Mater.* **2008**, *18*, 1057−1066.

(4) Rubloff, G. W.; Kozen, A. C.; Lee, S. B. From Nanoscience to Solutions in Electrochemical Energy Storage. *J. Vac. Sci. Technol., A* **2013**, *31*, 058503-1−058503-21.

(5) Park, M.; Zhang, X.; Chung, M.; Less, G. B.; Sastry, A. M. A Review of Conduction Phenomena in Li-ion Batteries. *J. Power Sources* **2010**, *195*, 7904−7929.

(6) Heitjans, P.; Indris, S. Diffusion and Ionic Conduction in Nanocrystalline Ceramics. *J. Phys.: Condens. Matter* **2003**, *15*, R1257−R1289.

(7) Zhang, H.; Yu, X.; Braun, P. V. Three-dimensional Bicontinuous Ultrafast-Charge and -Discharge Bulk Battery Electrodes. *Nat. Nanotechnol.* **2011**, *6*, 277−281.

(8) Valvo, M.; Roberts, M.; Oltean, G.; Sun, B.; Rehnlund, D.; Brandell, D.; Nyholm, L.; Gustafsson, T.; Edström, K. Electrochemical Elaboration of Electrodes and Electrolytes for 3D Structured Batteries. *J. Mater. Chem. A* **2013**, *1*, 9281−9293.

(9) Long, J. W.; Dunn, B.; Rolison, D. R.; White, H. S. Three-dimensional Battery Architectures. *Chem. Rev.* **2004**, *104*, 4463−4492.

(10) Oudenhoven, J. F. M.; Baggetto, L.; Notten, P. H. L. All-Solid-State Lithium-Ion Microbatteries: A Review of Various Three-Dimensional Concepts. *Adv. Energy Mater.* **2011**, *1*, 10−33.

(11) Cheng, F.; Liang, J.; Tao, Z.; Chen, J. Functional Materials for Rechargeable Batteries. *Adv. Mater.* **2011**, *23*, 1695−1715.

(12) Winter, M.; Besenhard, J.; Spahr, M. E.; Novak, P. Insertion Electrode Materials for Rechargeable Lithium Batteries. *Adv. Mater.* **1998**, *10*, 725−763.

(13) van der Ven, A.; Marianetti, C.; Morgan, D.; Ceder, G. Phase Transformations and Volume Changes in Spinel $LixMn_2O_4$. *Solid State Ionics* **2000**, *135*, 21−32.

(14) Kang, S.-H.; Goodenough, J.; Rabenberg, L. Nanocrystalline Lithium Manganese Oxide Spinel Cathode for Rechargeable Lithium Batteries. *Electrochem. Solid-State Lett.* **2001**, *4*, A49−A51.

(15) Kang, S.-H.; Goodenough, J. B.; Rabenberg, L. Effect of Ball Milling on 3-V Capacity of Lithium-Manganese Oxospinel Cathodes. *Chem. Mater.* **2001**, *13*, 1758−1764.

(16) Thackeray, M.; David, W.; Bruce, P.; Goodenough, J. Lithium Insertion into Manganese Spinels. *Mater. Res. Bull.* **1983**, *18*, 461−472.

(17) Thackeray, M. Manganese Oxides for Lithium Batteries. *Prog. Solid State Chem.* **1997**, *25*, 1−71.

(18) Gummow, R.; de Kock, A.; Thackeray, M. Improved Capacity Retention in Rechargeable 4 V Lithium/Lithiummanganese Oxide (Spinel) Cells. *Solid State Ionics* **1994**, *69*, 59−67.

(19) Striebel, K. A.; Rougier, A.; Horne, C.; Reade, R. P.; Cairns, E. J. Electrochemical Studies of Substituted Spinel Thin Films. *J. Electrochem. Soc.* **1999**, *146*, 4339−4347.

(20) Wang, H.; Jang, Y.-I.; Chiang, Y.-M. Origin of Cycling Stability in Monoclinic and Orthorhombic-phase Lithium Manganese Oxide Cathodes. *Electrochem. Solid-State Lett.* **1999**, *2*, 490−493.

(21) Chiang, Y.-M.; Sadoway, D. R.; Jang, Y.-I.; Huang, B.; Wang, H. High Capacity, Temperature-stable Lithum Aluminum Manganese Oxide Cathodes for Rechargeable Batteries. *Electrochem. Solid-State Lett.* **1999**, *30*, 107−110.

(22) Li, J.; Zhu, Y.; Wang, L.; Cao, C. Lithium Titanate Epitaxial Coating on Spinel Lithium Manganese Oxide Surface for Improving the Performance of Lithium Storage Capability. *ACS Appl. Mater. Interfaces* **2014**, *6*.1874210.1021/am504319y

(23) Esbenshade, J. L.; Fox, M. D.; Gewirth, A. A. $LiMn_2O_4$@Au Particles as Cathodes for Li-Ion Batteries. *J. Electrochem. Soc.* **2015**, *162*, A26−A29.

(24) Armstrong, M. J.; O'Dwyer, C.; Macklin, Z. J.; Holmes, J. D. Evaluating the Performance of Nanostructured Materials as Lithium-Ion Battery Electrodes. *Nano Res.* **2014**, *7*, 1−62.

(25) Okubo, M.; Mizuno, Y.; Yamada, H.; Kim, J.; Hosono, E.; Zhou, H.; Kudo, T.; Honma, I. Fast Li-ion Insertion into Nanosized $LiMn_2O_4$ Without Grain Boundaries. *ACS Nano* **2010**, *4*, 741−752.

(26) Ren, Y.; Armstrong, R.; Jiao, F.; Bruce, P. G. Influence of Size on the Rate of Mesoporous Electrodes for Lithium Batteries. *J. Am. Chem. Soc.* **2010**, *132*, 996−1004.

(27) Kim, D. K.; Muralidharan, P.; Lee, H.-W.; Ruffo, R.; Yang, Y.; Chan, C. K.; Peng, H.; Huggins, R. A.; Cui, Y. Spinel $LiMn_2O_4$ Nanorods as Lithium Ion Battery Cathodes. *Nano Lett.* **2008**, *8*, 3948−3952.

(28) Hosono, E.; Kudo, T.; Honma, I.; Matsuda, H.; Zhou, H. Synthesis of Single Crystalline Spinel $LiMn_2O_4$ Nanowires for a Lithium Ion Battery with High Power Density. *Nano Lett.* **2009**, *9*, 1045−1051.

(29) Lee, H.-W.; Muralidharan, P.; Ruffo, R.; Mari, C. M.; Cui, Y.; Kim, D. K. Ultrathin Spinel $LiMn_2O_4$ Nanowires as High Power Cathode Materials for Li-Ion Batteries. *Nano Lett.* **2010**, *10*, 3852−3856.

(30) Jiao, F.; Bao, J.; Hill, A. H.; Bruce, P. G. Synthesis of Ordered Mesoporous Li-Mn-O Spinel as a Positive Electrode for Rechargeable Lithium Batteries. *Angew. Chem., Int. Ed.* **2008**, *47*, 9711−9716.

(31) Bruce, P. G.; Scrosati, B.; Tarascon, J.-M. Nanomaterials for Rechargeable Lithium Batteries. *Angew. Chem., Int. Ed.* **2008**, *47*, 2930−2946.

(32) Maier, J. Nanoionics: Ion Transport and Electrochemical Storage in Con?ned Systems. *Nat. Mater.* **2005**, *4*, 805−815.

(33) Maier, J. Pushing Nanoionics to the Limits: Charge Carrier Chemistry in Extremely Small Systems. *Chem. Mater.* **2014**, *26*, 348−360.

(34) Thackeray, M. A comment on the Structure of Thin-Film $LiMn_2O_4$ Electrodes. *J. Electrochem. Soc.* **1997**, *144*, L100−L102.

(35) Wagemaker, M.; Borghols, W. J.; Mulder, F. M. Large Impact of Particle Size on Insertion Reactions. A case for Anatase TiO_2. *J. Am. Chem. Soc.* **2007**, *129*, 4323−4327.

(36) Okubo, M.; Hosono, E.; Kim, J.; Enomoto, M.; Kojima, N.; Kudo, T.; Zhou, H.; Honma, I. Nanosize effect on High-Rate Li-Ion Intercalation in LiCoO2 Electrode. *J. Am. Chem. Soc.* **2007**, *129*, 7444−7452.

(37) Miikkulainen, V.; Ruud, A.; Ostreng, E.; Nilsen, O.; Sajavaara, T.; Laitinen, M.; Fjellvag, H. Atomic Layer Deposition of Spinel Lithium Manganese Oxide by Film-?Body-?Controlle Lithium Incorporation for Thin-?Film Lithium-?Ion Batteries. *J. Phys. Chem. C* **2013**, *5*, 298−303.

(38) Liu, C.; Gillette, E. I.; Chen, X.; Pearse, A. J.; Kozen, A. C.; Schroeder, M. A.; Gregorczyk, K. E.; Lee, S. B.; Rubloff, G. W. An All-in-one Nanopore Battery Array. *Nat. Nanotechnol.* **2014**, *9*, 1031−1039.

(39) Yamada, A.; Tanaka, M. Jahn-Teller Structural Phase Transition around 280K in $LiMn_2O_4$. *Mater. Res. Bull.* **1995**, *30*, 715−721.

(40) Scherrer, P.; Göttinger, P. *Nachrichten Math. Phys.* **1918**, *2*, 98−100.

(41) Thackeray, M.; Mansuetto, M.; Bates, J. Structural Stability of $LiMn_2O_4$ Electrodes for Lithium Batteries. *J. Power Sources* **1997**, *68*, 153−158.

(42) Gummow, R.; Thackeray, M. An Investigation of Spinel-Realted and Orthorhombic $LiMnO_2$ Cathodes for Rechargeable Lithium Batteries. *J. Electrochem. Soc.* **1994**, *141*, 1178−1182.

(43) Yoshio, M.; Brodd, R. J.; Kozawa, A. *Lithium Ion Batteries;* Springer: New York, 2009.

(44) Dudney, N.; Bates, J.; Zuhr, R.; Young, S.; Robertson, J.; Jun, H.; Hackney, S. Nanocrystalline $LixMn_2$-yO_4 Cathodes for Solid-State Thin-Film Rechargeable Lithium Batteries. *J. Electrochem. Soc.* **1999**, *146*, 2455−2464.

(45) Kudo, T.; Hibino, M. Theoretical Dependences of the Free and Chemical Potential upon Composition in Intercalation Systems with Repulsive Interaction Between Guest Ions. *Electrochim. Acta* **1997**, *43*, 781−789.

(46) *Mechanical Stress on the Nanoscale: Simulation, Material Systems and Characterization Techniques;* Hanbucken, M., Muller, P., Wehrspohn, R. B., Eds.; Wiley VCH: Weinheim, Germany, 2011.

(47) Huggins, R.; Nix, W. Decrepitation Model For Capacity Loss During Cycling of Alloys in Rechargeable Electrochemical Systems. *Ionics* **2000**, *6*, 57−63.

(48) Bjork, M. T.; Ohlsson, B. J.; Sass, T.; Persson, A. I.; Thelander, C.; Magnusson, M. H.; Deppert, K.; Wallenberg, L. R.; Samuelson, L. One-dimensional Steeplechase for Electrons Realized. *Nano Lett.* **2002**, *2*, 87−89.

(49) Björk, M. T.; Ohlsson, B. J.; Sass, T.; Persson, A. I.; Thelander, C.; Magnusson, M. H.; Deppert, K.; Wallenberg, L. R.; Samuelson, L. One-dimensional Heterostructures in Semiconductor Nanowhiskers. *Appl. Phys. Lett.* **2002**, *80*, 1058−1060.

(50) Martensson, T.; Svensson, C. P. T.; Wacaser, B. A.; Larsson, M. W.; Seifert, W.; Deppert, K.; Gustafsson, A.; Wallenberg, L. R.; Samuelson, L. Epitaxial IIIV Nanowires on Silicon. *Nano Lett.* **2004**, *4*, 1987−1990.

(51) Muna, D.; Valvo, M.; van Erven, J.; Kelder, E. M.; Hassoun, J.; Panero, S. Silicon-based Nanocomposite for Advanced Thin Film Anodes in Lithium-Ion Batteries. *J. Mater. Chem.* **2012**, *22*, 1556−1561.

(52) Ebin, B.; Battaglia, V.; Gurmen, S. Comparison of 4V and 3V Electrochemical Properties of Nanocrystalline $LiMn_2O_4$ Cathode Particles in Lithium Ion Batteries Prepared by Ultrasonic Spray Pyrolysis. *Ceram. Int.* **2014**, *40*, 7029−7035.

(53) Mohamedi, M.; Takahashi, D.; Itoh, T.; Umeda, M.; Uchida, I. ESD Fabricated Thin Films of Spinel$LiMn_2O_4$ for Lithium Micro-batteries. *J. Electrochem. Soc.* **2002**, *149*, A19−A25.

(54) Inaguma, Y.; Liquan, C.; Itoh, M.; Nakamura, T.; Uchida, T.; Ikuta, H.; Wakihara, M. High Ionic Conductivity in Lithium Lanthanum Titanate. *Solid State Commun.* **1993**, *86*, 689−693.